Satellite-Transition MAS NMR of Spin I = 3/2, 5/2, 7/2, and 9/2 Nuclei: Sensitivity, Resolution, and Practical Implementation

Sharon E. Ashbrook and Stephen Wimperis[1]

School of Chemistry, University of Exeter, Stocker Road, Exeter EX4 4QD, United Kingdom

The satellite-transition MAS (STMAS) experiment offers an alternative approach to established methods such as dynamic angle spinning (DAS), double rotation (DOR), and multiple-quantum MAS (MQMAS) for obtaining high-resolution NMR spectra of half-integer quadrupolar nuclei. Unlike the multiple-quantum experiment, STMAS involves two-dimensional correlation of purely single-quantum coherences; satellite transitions in t_1 (or F_1) and the central transition in t_2 (or F_2). To date, STMAS has primarily been demonstrated for nuclei with spin quantum numbers $I = 3/2$ and, to a lesser extent, $I > 5/2$. However, many chemically relevant nuclei possess $I > 3/2$, such as ^{17}O and ^{27}Al (both $I = 5/2$), ^{59}Co ($I = 7/2$), and ^{93}Nb ($I = 9/2$). Here, we discuss the application of STMAS to nuclei with spin quantum numbers from $I = 3/2$ to $9/2$. First, we consider the practical implementation of the STMAS experiment using ^{87}Rb ($I = 3/2$) NMR as an example. We then extend the discussion to include nuclei with higher spin quantum numbers, demonstrating ^{27}Al, ^{45}Sc ($I = 7/2$), ^{59}Co, and ^{93}Nb STMAS experiments on both crystalline and amorphous samples. We also consider the possibility of experiments involving satellite transitions other than $m_I = \pm 1/2 \leftrightarrow \pm 3/2$ and, using ^{93}Nb NMR, demonstrate the correlation of all single-quantum satellite transitions up to and including $m_I = \pm 7/2 \leftrightarrow \pm 9/2$. The absolute chemical shift scaling factors in these experiments are discussed, as are the implications for isotropic resolution.   © 2002 Elsevier Science (USA)

INTRODUCTION

Although the dynamic angle spinning (DAS) (*1*) and double rotation (DOR) (*2*) techniques have been used since 1988 to obtain high-resolution NMR spectra of half-integer quadrupolar nuclei, their wider impact has been limited by their technical complexity. In contrast, the more recent multiple-quantum MAS (MQMAS) experiment of Frydman and Harwood (*3*) has found extensive application owing to the ease of its implementation. The ability to excite and convert multiple-quantum coherences with high efficiency is crucial to the successful use of this experiment. However, despite the progress made in improving the coherence transfer efficiencies (*4–6*), this aspect of the MQMAS technique remains its biggest limitation.

The satellite-transition MAS (STMAS) experiment, introduced by Gan in 2000 (*7*), offers an alternative approach for the acquisition of high-resolution NMR spectra of half-integer quadrupolar nuclei, involving the correlation of purely single-quantum satellite (ST) and central (CT) transitions in a two-dimensional experiment performed under MAS conditions. Rotor-synchronized acquisition must be employed as, unlike the central transition or indeed many multiple-quantum transitions, the satellite transitions are not inherently free from first-order quadrupolar broadening. The second-order quadrupolar broadenings of the satellite and central transitions differ by a simple scaling factor and, therefore, a high-resolution or "isotropic" spectrum may be obtained by two-dimensional correlation.

The STMAS method has been demonstrated for spin $I = 3/2$ and $I = 5/2$ nuclei and, in comparison with MQMAS, impressive time savings have been achieved (*8, 9*). However, for nuclei with spin quantum number $I > 3/2$, more than one pair of satellite transitions exist (ST$_1$ with $m_I = \pm 1/2 \leftrightarrow \pm 3/2$, ST$_2$ with $m_I = \pm 3/2 \leftrightarrow \pm 5/2$, etc.) and these, unlike the multiple-quantum coherence orders excited in MQMAS experiments, cannot be separated by phase cycling. Consequently, a two-dimensional STMAS spectrum may contain a significant number of correlation peaks. Many nuclei of industrial, geological, and biological relevance, such as ^{17}O and ^{27}Al (both $I = 5/2$), ^{59}Co ($I = 7/2$), and ^{93}Nb ($I = 9/2$), possess $I > 3/2$ and, therefore, application of STMAS to nuclei with high spin quantum numbers is of great importance (*10*).

In this paper, we discuss the use of STMAS for nuclei with spin quantum numbers between $I = 3/2$ and $9/2$. First, we briefly consider the experimental requirements for implementing the STMAS technique, such as very accurate setting of the magic angle, the optimization of pulse durations, and the choice of pulse sequence. The application of STMAS to higher spin nuclei, such as ^{27}Al, ^{45}Sc ($I = 7/2$), ^{59}Co, and ^{93}Nb, is then demonstrated and the possibility of performing experiments using the higher order satellite transitions is shown. The dispersion of isotropic frequency shifts achieved in these experiments and the resulting implications for spectral resolution are considered.

[1] To whom correspondence should be addressed. Fax: +44-1392-263434. E-mail: s.wimperis@exeter.ac.uk.

EXPERIMENTAL CONSIDERATIONS

The original STMAS pulse sequences proposed by Gan included a two-pulse sequence and a three-pulse z-filtered sequence (7). Recently, a three-pulse shifted-echo sequence, as shown in Fig. 1a, that yields purely absorptive two-dimensional lineshapes has been employed (9, 11, 12). The third pulse in this sequence has a much reduced amplitude and acts as a selective inversion pulse across the central transition. After complex (i.e., not real or hypercomplex) Fourier transformation, each $ST_n \rightarrow CT$ ridge-like correlation peak in the spectrum has a gradient corresponding to the ratio of the second-order quadrupolar broadenings of the ST_n and CT transitions. These STMAS ratios, $R(I, q)$, are given, for all relevant spin quantum numbers I and satellite transitions $m_I = \pm(q - 1) \leftrightarrow \pm q$, in Table 1. A one-dimensional high-resolution or isotropic spectrum may be obtained by projecting the two-dimensional spectrum onto an axis orthogonal to the STMAS gradient.

The incorporation of a split-t_1 evolution period (13–16) into the three-pulse sequence, as shown in Fig. 1b, has also been demonstrated (9). By splitting the t_1 evolution period into two parts and setting the ratio of their durations equal to the relevant STMAS ratio, a $ST_n \rightarrow CT$ ridge will appear parallel to the F_2 axis without the need for a shearing transformation. The positioning of the second (CT) part of the t_1 evolution period, either before or after the final pulse as shown in Fig. 1b, is dependent upon the sign of the STMAS ratio (given in Table 1). For $ST_n \rightarrow CT$ correlations with a negative $R(I, q)$, such as $ST_1 \rightarrow CT$ for spin $I = 3/2$ nuclei, the second t_1 evolution period is placed before the final pulse (i.e., $k'' = 0$ in Fig. 1b). If the STMAS ratio is positive, e.g., $ST_1 \rightarrow CT$ for $I = 5/2$, the second t_1 evolution period occurs after the final pulse (i.e., $k' = 0$ in Fig. 1b).
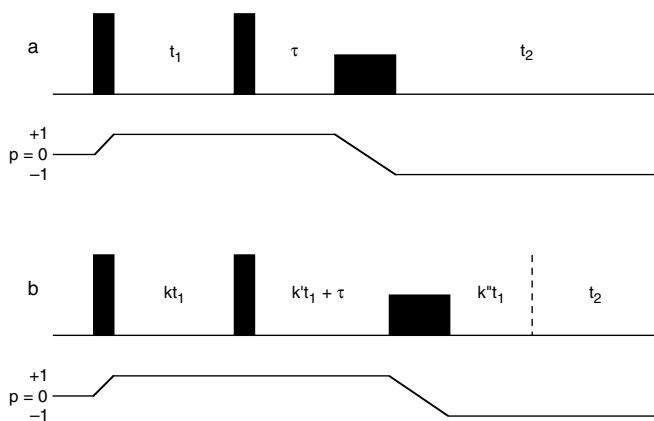

FIG. 1. Pulse sequence and coherence transfer pathways for (a) three-pulse shifted-echo STMAS experiment and (b) split-t_1 shifted-echo STMAS experiment. In (b), k, k', and k'' are chosen to refocus the second-order quadrupolar broadening at the end of the t_1 period. In each experiment, a 32-step phase cycle can be used to select the desired coherence pathways: 1st pulse, 0°; 2nd pulse, 0° 45° 90° 135° 180° 225° 270° 315°; 3rd pulse, 8(0°) 8(90°) 8(180°) 8(270°); receiver, 8(0°)–8(180°).

TABLE 1

STMAS Ratios, $R(I, q)$, as a Function of Spin Quantum Number I and Transition Label q, where the Satellite Transition is $m_I = \pm(q - 1) \leftrightarrow \pm q$

I	q	$R(I, q)$
3/2	3/2	−8/9
5/2	3/2	7/24
	5/2	−11/6
7/2	3/2	28/45
	5/2	−23/45
	7/2	−108/45
9/2	3/2	55/72
	5/2	1/18
	7/2	−9/8
	9/2	−25/9

Although the central transition is free from first-order quadrupolar broadening, rotor-synchronized acquisition is necessary in t_1 to remove the first-order broadening of the satellite transitions. This is achieved in the sequence in Fig. 1a by setting the increment of the t_1 evolution time equal to the MAS rotor period, τ_R, so that an F_1 spectral width equal to ν_R, the MAS rate, is obtained (7, 8). For the split-t_1 sequence in Fig. 1b a rotor-synchronized spectrum is obtained by setting the increment of the kt_1 period equal to τ_R (9). The use of half-rotor synchronization to obtain a high-resolution spectrum free from the unwanted $CT \rightarrow CT$ peak was recently demonstrated (9). In this case, the increment of the t_1 or kt_1 period is set equal to half of the rotor period, i.e., $\tau_R/2$, leading to a doubling of the F_1 spectral width. This method can be viewed as an interleaved (in t_1) version of one more recently proposed by Gan that involves subtraction of a second, nonsynchronized experiment (17); being essentially identical, both methods lead to a reduction in the signal-to-noise ratio per unit time by a factor of 2.

Experiments were performed on Bruker Avance 400 and 200 spectrometers operating at static magnetic field strengths, B_0, of 9.4 and 4.7 T, respectively. Conventional Bruker MAS probeheads were used with powdered samples packed inside either 2.5-mm (Avance 400) or 4-mm (Avance 200) rotors. Spinning rates between 10 and 33.3 kHz were used. The presence of the first-order quadrupolar interaction in the satellite transitions results in an extreme sensitivity to the magic angle setting. Although these splittings are removed by a combination of MAS and rotor synchronization, any small deviation from the magic angle reintroduces the first-order interaction and $ST_n \rightarrow CT$ peaks are no longer narrow ridges, but exhibit a correlation of first- and second-order quadrupolar broadenings (8). Accurate setting of the magic angle is, therefore, essential to the success of the STMAS experiment. In our experiments the magic angle is set to an estimated accuracy of 54.736° ± 0.004°, first, by optimization of the number and amplitude of rotary echoes in a normal FID and, subsequently, by maximizing the height of the
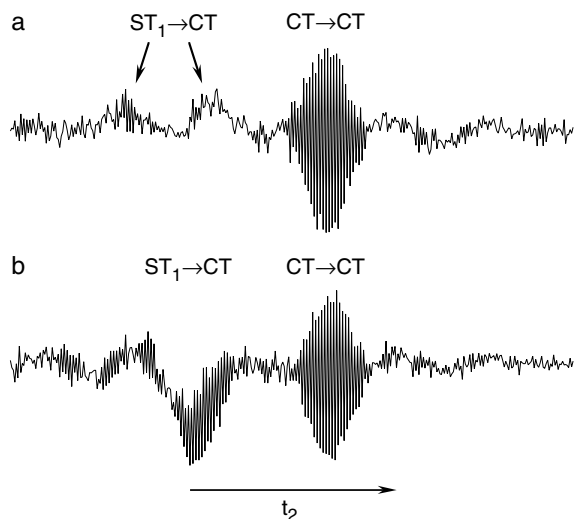
FIG. 2. ^{87}Rb (130.9 MHz) NMR of RbNO$_3$. Shifted-echo STMAS FID recorded using the pulse sequence in Fig. 1a with a finite t_1 period, (a) prior to and (b) following the setting of the magic angle using the ST$_1 \rightarrow$ CT shifted-echo intensity.

ST$_1 \rightarrow$ CT shifted-echo signal observed in a one-dimensional STMAS experiment. Figure 2a shows a ^{87}Rb ($I = 3/2$) FID of RbNO$_3$, recorded using the pulse sequence in Fig. 1a with a finite t_1 value, before the setting of the magic angle. Two echoes are observed: the CT $\rightarrow$ CT echo refocused at the longer t_2 value and the ST$_1 \rightarrow$ CT (anti)echo signal refocused at the shorter t_2 value. Although a large CT $\rightarrow$ CT signal is observed, the ST$_1 \rightarrow$ CT signal is small and appears, owing to the missetting of the magic angle, to be split into two separate parts. The FID in Fig. 2b, recorded after the magic angle has been corrected, shows a single, much more intense ST$_1 \rightarrow$ CT (anti)echo.

In addition to ST$_n \rightarrow$ CT peaks, a two-dimensional STMAS experiment resulting from the application of the pulse sequences in Fig. 1 will also contain unwanted CT $\rightarrow$ CT peaks lying along the auto-correlation diagonal. These unresolved peaks may pose problems in STMAS spectra, particularly for nuclei with spin $I > 3/2$, as the resolution of the central transition relative to the inner (ST$_1$) satellite transitions decreases rapidly as the spin quantum number increases. "Presaturation" of the central transition has been suggested, although true presaturation is difficult to achieve experimentally (7, 8). Recently, we employed half-rotor synchronization to attempt to overcome this problem (9); however, as with the method of Gan (17), this approach is not successful in samples where the central transition also exhibits strong spinning sidebands.

Alternatively, the amplitude of the CT $\rightarrow$ CT coherence transfer step may be reduced relative to those of the ST$_n \rightarrow$ CT steps by careful selection of the pulse durations. Figures 3a and 3b show contour plots of STMAS FIDs (shown in magnitude mode) as a function of pulse duration. These time-domain ^{87}Rb ($I = 3/2$) data were recorded using the three-pulse shifted-echo sequence shown in Fig. 1a with a finite t_1 period. Figure 3a, plot-

ted as a function of the duration of the first pulse, $p1$, in this sequence with the second, $p2$, equal to 1.0 μs, reveals that the maximum CT $\rightarrow$ CT signal intensity is obtained with $p1 \approx 1.1\ \mu$s, while the maximum ST$_1 \rightarrow$ CT signal intensity is obtained with $p1 \approx 1.4\ \mu$s. However, it can be seen that a minimum in CT $\rightarrow$ CT intensity is obtained at longer $p1$ values ($p1 \approx 2.4\ \mu$s) without significant loss in the intensity of the ST$_1 \rightarrow$ CT coherence transfer echo. Figure 3b, plotted as function of the $p2$ duration with $p1 = 2.4\ \mu$s, shows that $p2 \approx 1.5\ \mu$s results in the maximum intensity of the ST$_1 \rightarrow$ CT signal and the minimum CT $\rightarrow$ CT signal. This is confirmed in a more conventional format in Figs. 3c and 3d. Figure 3c shows a ^{87}Rb FID, with an initial pulse duration of 1.4 μs, resulting in an amplitude close to a maximum for both CT $\rightarrow$ CT and ST$_1 \rightarrow$ CT echo signals. However, the relative intensities of the two may be altered significantly through the use of a longer first pulse duration (2.4 μs), as shown in Fig. 3d, at little cost to the ST$_1 \rightarrow$ CT intensity.

SENSITIVITY AND RESOLUTION

Although both STMAS and MQMAS involve two-dimensional correlation under MAS conditions, the purely single-quantum STMAS experiment is expected to have significant sensitivity advantages over MQMAS as a result of the relative inefficiency of multiple-quantum excitation and conversion. Figures 4a and 4b compare isotropic ^{87}Rb STMAS and MQMAS NMR spectra of RbNO$_3$. The STMAS spectrum (Fig. 4a) was recorded in only 32 min and yet the isotropic peaks are approximately 1.6 times more intense than those observed in an MQMAS spectrum (Fig. 4b) recorded in 100 min with the same limiting resolution in both dimensions. Per unit experiment time, this corresponds to a relative sensitivity advantage of a factor of 4.8 for STMAS. Note, however, that the "noise" in the isotropic STMAS projection appears larger as a result of both the presence of the unwanted CT $\rightarrow$ CT peak and an increase in "t_1 noise" (18) arising from instabilities in the MAS rate. Figures 4c and 4d, showing cross-sections along one of the ^{87}Rb ridge lineshapes and taken from two-dimensional STMAS and MQMAS spectra, respectively, display a second-order broadened quadrupolar lineshape with quadrupolar coupling constant $C_Q = 1.74$ MHz and asymmetry $\eta = 0.5$ (12). The STMAS cross-section (Fig. 4c) is now free from the t_1 noise inherent in the isotropic projection in Fig. 4a and can be seen to have a better signal-to-noise ratio than the MQMAS cross-section (Fig. 4d) despite being recorded in only a third of the time.

In addition to a relative signal enhancement resulting from its purely single-quantum nature, the STMAS experiment possesses a further significant sensitivity advantage over MQMAS at high spinning rates. Figure 5a shows the effect of the MAS rate upon the amplitude of spin $I = 3/2$ satellite and triple-quantum coherences as a function of the pulse duration. Simulations were performed for an on-resonance excitation pulse with a radiofrequency field strength of $\omega_1/2\pi = 100$ kHz, with $C_Q = 2$ MHz and $\eta = 0$. For STMAS, although a decrease in signal intensity
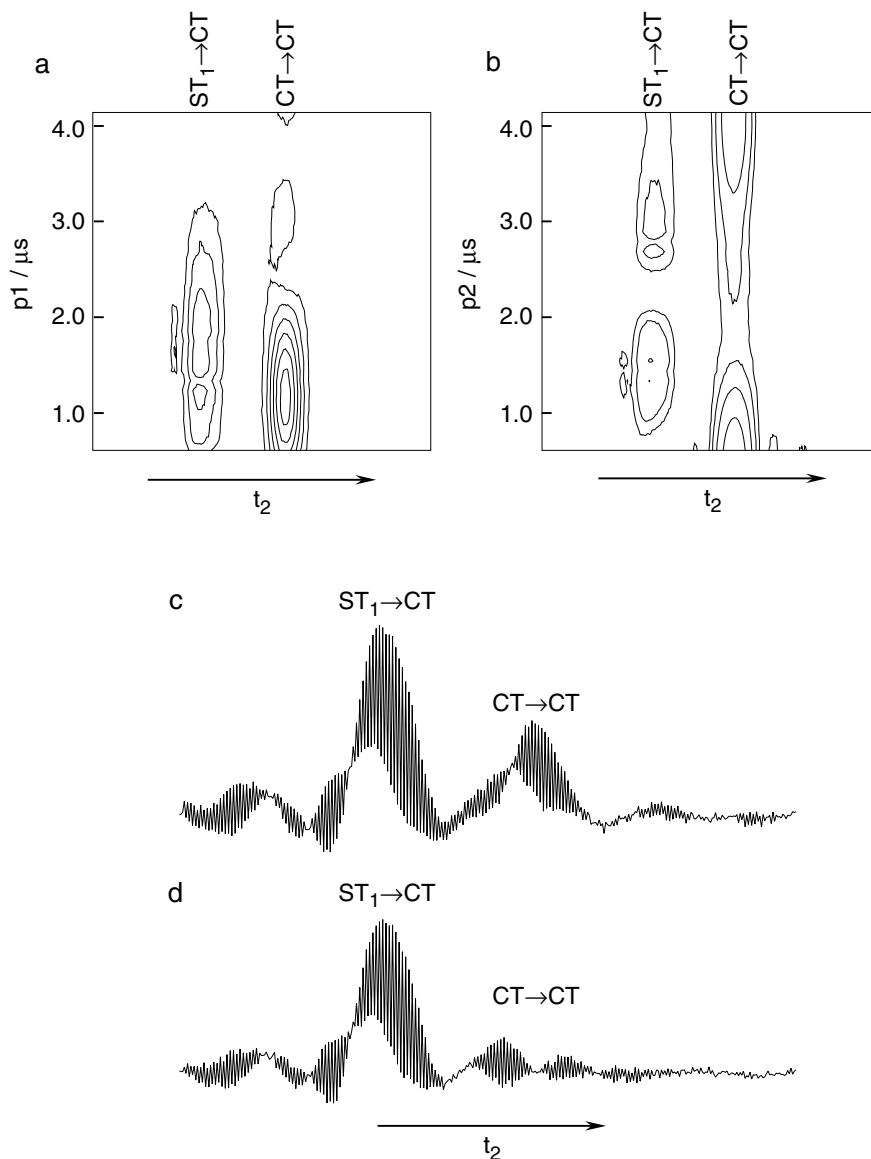
FIG. 3. [87]Rb (130.9 MHz) NMR of RbNO$_3$. Shifted-echo STMAS FIDs recorded using the pulse sequence in Fig. 1a with a finite t_1 period. (a) and (b) Contour plots of magnitude-mode FIDs as a function of the first and second pulse durations, respectively. In (a) the second pulse duration ($p2$) was fixed at 1.0 μs, whilst in (b) the first pulse duration ($p1$) was fixed at 2.4 μs. (c) and (d) FIDs recorded with (c) $p1 = 1.4$ μs and $p2 = 1.5$ μs and (d) $p1 = 2.4$ μs and $p2 = 1.5$ μs; the CT $\rightarrow$ CT echo is much reduced in intensity relative to the ST$_1 \rightarrow$ CT echo in (d).

is observed with increasing MAS rate at longer pulse durations, the maximum signal intensity, found at $\sim$1 μs, remains independent of the MAS rate. However, for MQMAS, it can be seen that the maximum amplitude of triple-quantum excitation, found at $\sim$7 μs, decreases significantly as the MAS rate increases (*19*). The MAS rate can be shown to have much less effect upon the conversion of both triple-quantum and satellite coherences into single-quantum coherences, as the maximum amplitude of both is obtained at shorter pulse durations (*20*).

The simulations in Fig. 5a predict that the sensitivity advantage of STMAS over MQMAS may be expected to increase as the MAS rate increases. This is confirmed experimentally in Fig. 5b

where the amplitudes of [87]Rb satellite and triple-quantum coherences in RbNO$_3$ are plotted as a function of the pulse duration for a range of spinning rates. The amplitude of the satellite coherences remains fairly constant as the MAS rate is increased from 10 to 30 kHz, with a maximum obtained at $\sim$1.8 μs in all cases. However, for the excitation of triple-quantum coherences a significant decrease in signal amplitude is observed at high MAS rates. At lower spinning speeds, between 0 and 10 kHz, the amplitude of the triple-quantum coherences excited remains fairly constant.

The high-resolution or isotropic spectra shown in Figs. 4a and 4b are obtained from a two-dimensional STMAS or MQMAS
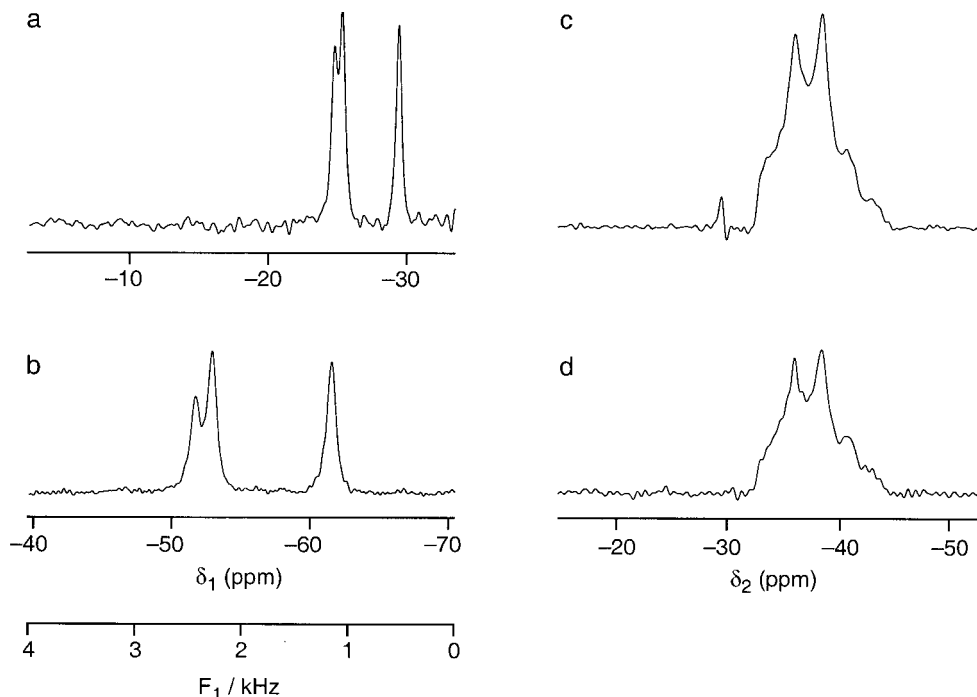
FIG. 4. ^{87}Rb (130.9 MHz) NMR of RbNO$_3$. (a) and (b) Isotropic projections and (c) and (d) cross-sections parallel to δ_2 axis taken from two-dimensional (a) and (c) STMAS and (b) and (d) triple-quantum MAS spectra, recorded with (a) and (c) the split-t_1 pulse sequence in Fig. 1b with $k = 9/17$, $k' = 8/17$, and $k'' = 0$, and (b) and (d) a triple-quantum split-t_1 pulse sequence (14). In (a) and (c) 32 and (b) and (d) 96 transients were averaged with a recycle interval of 250 ms for each of 256 t_1 increments of 94.4 μs. The MAS rate was 20 kHz. All ppm scales are referenced relative to 1 M RbNO$_3$ (aq), while the additional F_1 scale shows the offset from the transmitter frequency in units of kHz.
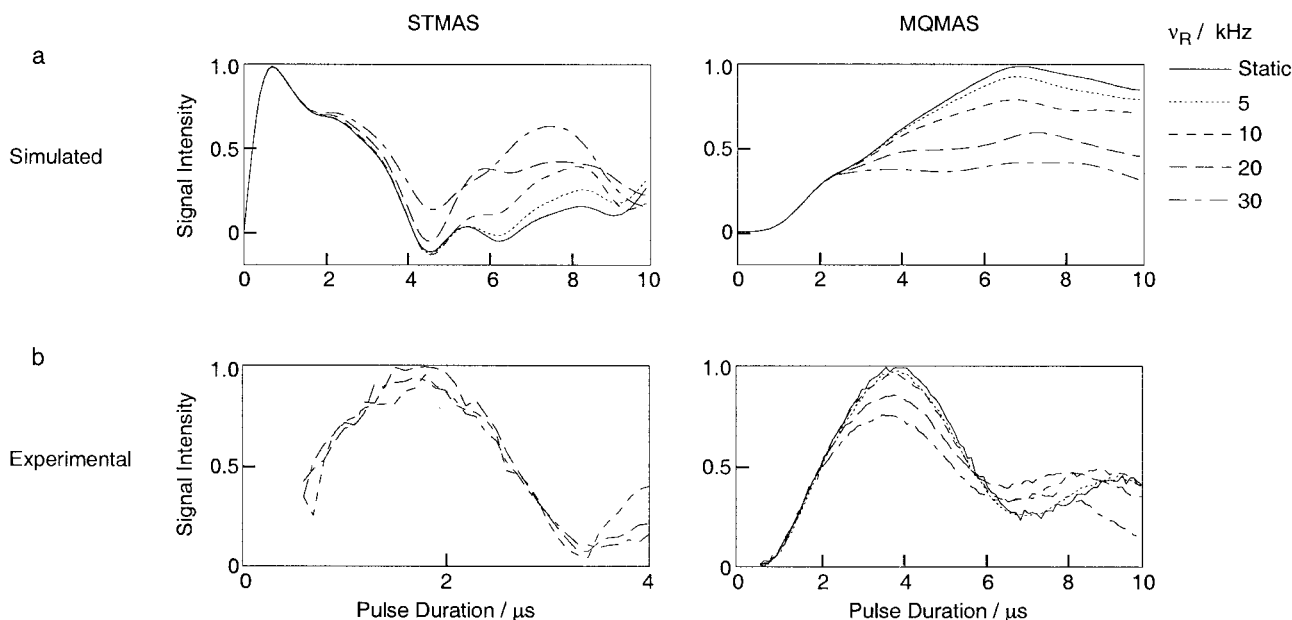

FIG. 5. (a) The effect of MAS upon the amplitude of $I = 3/2$ satellite and triple-quantum coherences as a function of the excitation pulse duration. Simulations were performed for an on-resonance excitation pulse with a radiofrequency field strength, $\omega_1/2\pi$, of 100 kHz, with $C_Q = 2$ MHz and $\eta = 0$. (b) The effect of MAS upon the amplitude of ^{87}Rb (130.9 MHz) satellite and triple-quantum coherences of RbNO$_3$ as a function of the excitation pulse duration (estimated radiofrequency field strength $\omega_1/2\pi \approx 160$ kHz). For STMAS experiments, 128 transients were averaged with a recycle interval of 250 ms with a reconversion pulse of 1.5 μs, while for triple-quantum MAS experiments 96 transients were averaged with a recycle interval of 250 ms and a reconversion pulse of 1.2 μs. In each case, the vertical scale is in arbitrary units and MAS rates of 0, 5, 10, 20, and 30 kHz are denoted by solid, dotted, dashed, long-dashed, and dot-dashed lines, respectively.

TABLE 2

Absolute Chemical Shift Scaling Factors, $|x_{CS}(I, q)|$ and $|x_{CS}(I, p)|$, for Isotropic STMAS and MQMAS Spectra as a Function of Spin Quantum Number I, Transition Label q (STMAS), and Coherence Order, p (MQMAS)

	STMAS		MQMAS	
I	q	$|x_{CS}(I, q)|$	$|p|$	$|x_{CS}(I, p)|$
3/2	3/2	1.000	3	2.125
5/2	3/2	0.548	3	0.548
5/2	5/2	1.000	5	2.297
7/2	3/2	0.233	3	0.233
7/2	5/2	1.000	5	1.700
7/2	7/2	1.000	7	2.311
9/2	3/2	0.134	3	0.134
9/2	5/2	0.895	5	0.649
9/2	7/2	1.000	7	4.760
9/2	9/2	1.000	9	2.297

spectrum by calculating a projection onto an axis orthogonal to the ridge lineshapes. When measured in absolute frequency units, such as Hz, the isotropic shifts observed are inherently scaled relative to those found in a conventional MAS spectrum (*9, 21*). The isotropic chemical shift scaling factor for STMAS is given by

$$x_{CS}(I, q) = \frac{1 - R(I, q)}{1 + |R(I, q)|}, \qquad [1]$$

where q labels the satellite transitions ($m_I = \pm(q - 1) \to \pm q$) used in the experiment and $R(I, q)$ is the STMAS ratio, given in Table 1. The STMAS isotropic chemical scaling factors, $x_{CS}(I, q)$, are given in Table 2 along with the equivalent MQMAS scaling factors, $x_{CS}(I, p)$ (*21*). It is important to note that we do not attempt to "undo" or compensate for this inherent scaling of the isotropic shifts by introducing an artificial rescaling of the ppm or Hz axes: our ppm scales are calculated relative to the Larmor frequency $\omega_0/2\pi$ in the normal, IUPAC-approved fashion and our scales in Hz (an absolute frequency unit) have not been altered. The practice of axis scaling has been the cause of considerable confusion about isotropic resolution in MQMAS (which we have attempted to clear up in Ref. *21*) and it is to be hoped that this is not repeated with STMAS.

Table 2 shows that for spin $I = 3/2$ the chemical shift dispersion obtained in an STMAS experiment is $1/2.125 = 0.407$ of that obtained in a triple-quantum MAS spectrum. This corresponds to the different frequency dispersions seen in the isotropic ^{87}Rb STMAS and MQMAS spectra in Figs. 4a and 4b, where the shifts of the resonances away from the transmitter frequency (labeled in kHz) in the STMAS spectrum (Fig. 4a) are 0.407 times those in the MQMAS spectrum (Fig. 4b). However, the increased chemical shift dispersion obtained in the MQMAS spectrum is not fully translated into an increase in resolution owing to an increase in the linewidths of the MQMAS isotropic peaks (*21*). Nevertheless, some improvement in resolution is obtained in the MQMAS spectrum, owing in part to factors which may contribute additionally to the STMAS linewidth, such as a
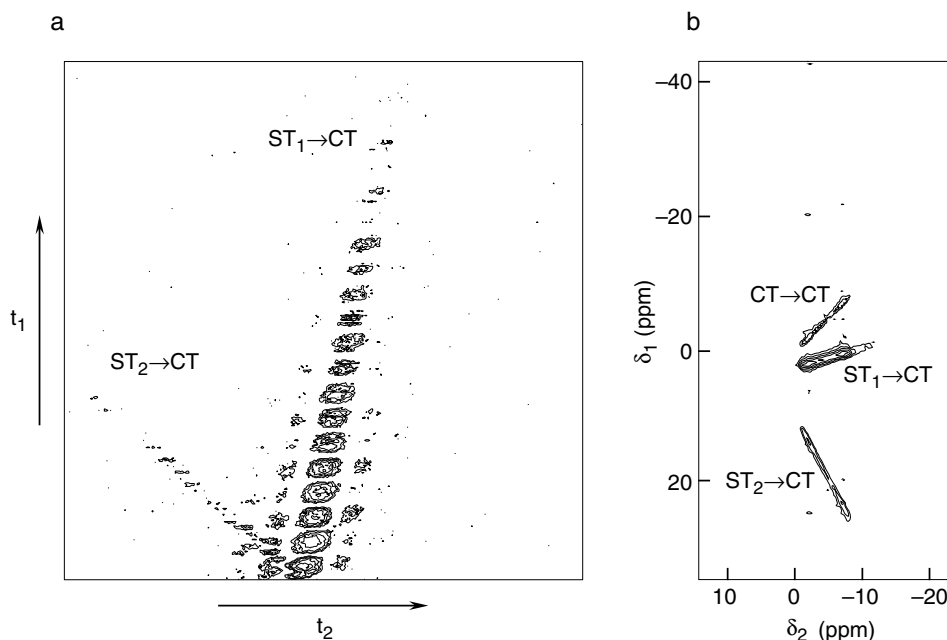

FIG. 6. ^{27}Al (104.3 MHz) NMR of aluminium acetylacetonate, Al(acac)$_3$. (a) Two-dimensional time-domain data set and (b) corresponding two-dimensional STMAS spectrum recorded using the pulse sequence shown in Fig. 1a. The spectrum is the result of the averaging of 32 transients with a recycle interval of 1 s for each of 512 t_1 increments of 50 μs. The MAS rate was 20 kHz. In (a) negative contour levels are omitted for clarity, whilst in (b) contour levels are shown at 4, 8, 16, 32, and 64% of the maximum intensity. The ppm scales are referenced to 1 M Al(NO$_3$)$_3$.

small missetting of the magic angle or small variations in spinning speed.

For nuclei with spin quantum number $I > 3/2$, Table 2 reveals that the $ST_1 \rightarrow CT$ isotropic spectrum has the same frequency dispersion as the triple-quantum isotropic spectrum and the spectral resonances will, therefore, occur at identical shifts (in Hz) from the transmitter frequency. However, when higher order satellite coherences, $ST_2 \rightarrow CT$, $ST_3 \rightarrow CT$, and $ST_4 \rightarrow CT$, are considered different scaling factors are obtained, although the maximum scaling factor in any STMAS experiment is 1.000.

STMAS OF SPIN $I = 5/2$ NUCLEI

For nuclei with spin quantum number $I = 5/2$, there are two types of satellite transition: ST_1 with $m_I = \pm 1/2 \leftrightarrow \pm 3/2$ and ST_2 with $m_I = \pm 3/2 \leftrightarrow \pm 5/2$, available for STMAS experiments. Consideration of Table 1 shows that the corresponding STMAS ratios of the two are different and, in particular, of differing sign. Figure 6a shows a two-dimensional ^{27}Al STMAS time-domain data set of aluminium acetylacetonate, Al(acac)$_3$, which has a single crystallographic Al site (22), recorded using the shifted-echo pulse sequence in Fig. 1a. Only positive contour levels are shown, with negative contour levels omitted for clarity. Three echoes are expected, corresponding to CT $\rightarrow$ CT, $ST_1 \rightarrow CT$, and $ST_2 \rightarrow CT$ coherence transfer, although the CT $\rightarrow$ CT signal is present with only a small intensity and not observable on the contour levels shown. The CT $\rightarrow$ CT and $ST_1 \rightarrow CT$ signals, both with a positive STMAS ratio, are echo signals and move forward in t_2 as t_1 increases. However, the $ST_2 \rightarrow CT$ (anti)echo moves backward in t_2 with increasing t_1. Figure 6b shows the resulting two-dimensional spectrum where,
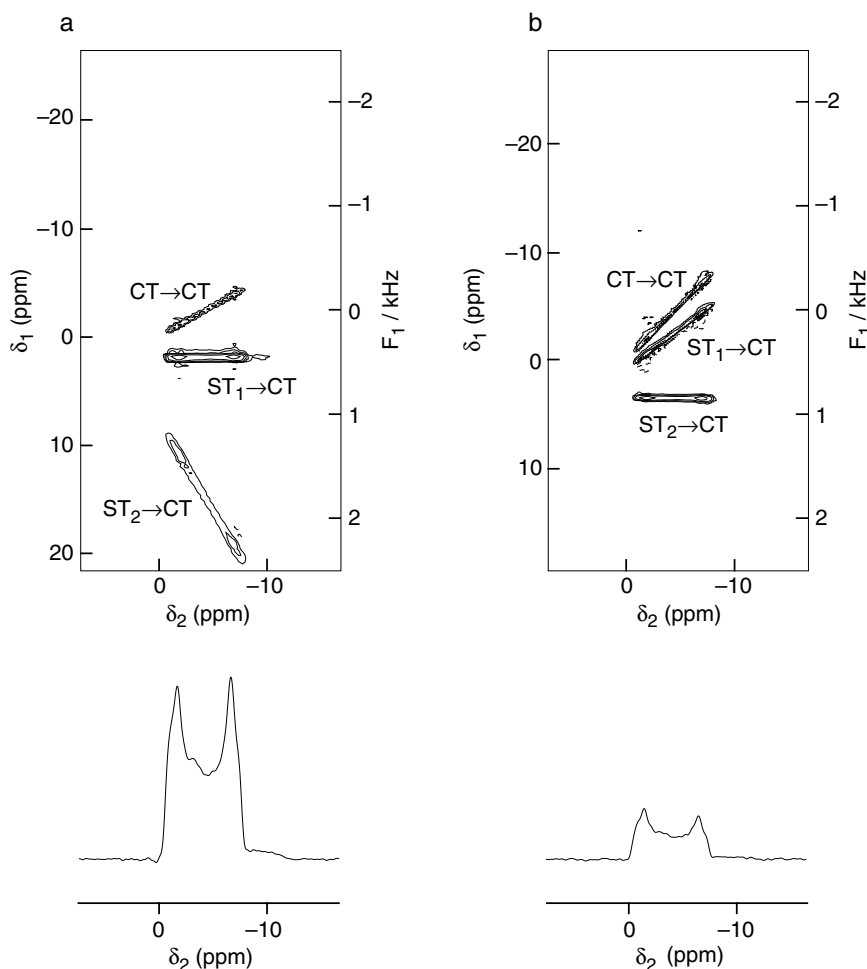

FIG. 7. ^{27}Al (104.3 MHz) NMR of aluminium acetylacetonate, Al(acac)$_3$. Two-dimensional STMAS spectra recorded using the split-t_1 pulse sequence shown in Fig. 1b, with (a) $k = 24/31$, $k' = 0$, and $k'' = 7/31$ and (b) $k = 6/17$, $k' = 11/17$, and $k'' = 0$. In each case, 64 transients were averaged with a recycle interval of 1 s for each of 256 t_1 increments of (a) 64.8 μs and (b) 141.6 μs. The MAS rate was 20 kHz. Contour levels are shown at (a) 4, 8, 16, 32, and 64% and (b) 8, 16, 32, and 64% of the maximum intensity. All ppm scales are referenced to 1 M Al(NO$_3$)$_3$, while the additional F_1 scale denotes the offset from the transmitter frequency in kHz. The cross-sections though the ridge lineshapes parallel to δ_2 illustrate the sensitivity difference between the $ST_1 \rightarrow CT$ and the $ST_2 \rightarrow CT$ experiments.
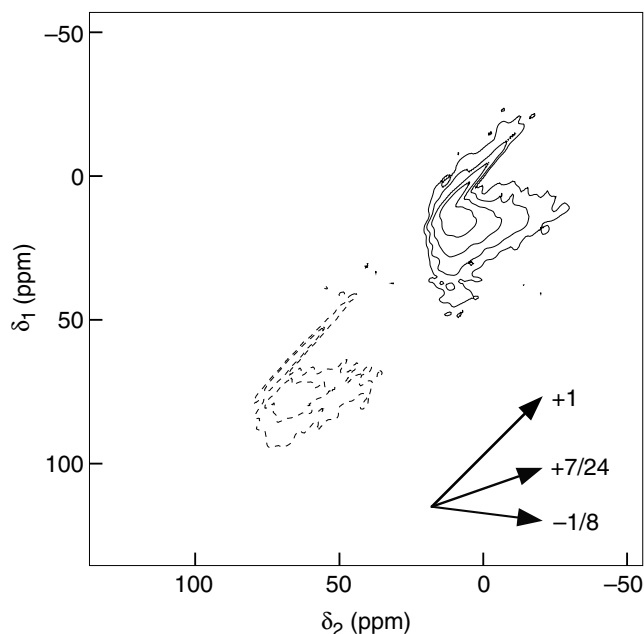
FIG. 8. ^{27}Al (104.3 MHz) NMR of γ-Al$_2$O$_3$. Two-dimensional STMAS spectrum recorded using the pulse sequence shown in Fig. 1a. The spectrum is the result of the averaging of 32 transients with a recycle interval of 1 s for each of 128 t_1 increments of 33.3 μs. The MAS rate was 30 kHz. Contour levels are shown at 8, 16, 32, and 64% of the maximum intensity. All ppm scales are referenced to 1 M Al(NO$_3$)$_3$.

in addition to the CT $\rightarrow$ CT peak lying along a gradient of $+1$, two other ridge lineshapes are observed, the ST$_1$ $\rightarrow$ CT peak along $+7/24$ and the ST$_2$ $\rightarrow$ CT peak along $-11/6$, confirming the $R(I, q)$ values in Table 1.

Figure 7 shows two-dimensional ^{27}Al STMAS NMR spectra of Al(acac)$_3$, recorded with the split-t_1 pulse sequence shown in Fig. 1b, together with cross-sections along the ^{27}Al ridge lineshape that lies parallel to δ_2. In Fig. 7a, the ST$_1$ $\rightarrow$ CT ridge occurs parallel to δ_2, while, in Fig. 7b, the ST$_2$ $\rightarrow$ CT ridge is parallel to δ_2. These two peaks occur at F_1 shifts of $+0.475$ and $+0.850$ kHz away from the transmitter frequency in Figs. 7a and 7b, respectively, reflecting the predicted difference in absolute scaling factor of 0.548 : 1 shown in Table 2. The cross-sections along the ^{27}Al ridge lineshape shown below the two-dimensional spectra illustrate the sensitivity difference between the ST$_1$ $\rightarrow$ CT and the ST$_2$ $\rightarrow$ CT experiments, with that in Fig. 7a possessing a signal intensity that is a factor of 4.2 times greater than that in Fig. 7b (note that the pulse durations were optimized in each experiment for the peak of interest). The decrease in sensitivity as the satellite transition label q increases is a general observation for nuclei with $I = 5/2$, 7/2, and 9/2.

The study of amorphous or disordered materials using high-resolution ^{27}Al NMR techniques such as MQMAS or STMAS is of considerable interest (23–26). Figure 8 shows a two-dimensional ^{27}Al ($I = 5/2$) STMAS spectrum of γ-Al$_2$O$_3$, recorded with the pulse sequence in Fig. 1a. Two ^{27}Al signals are

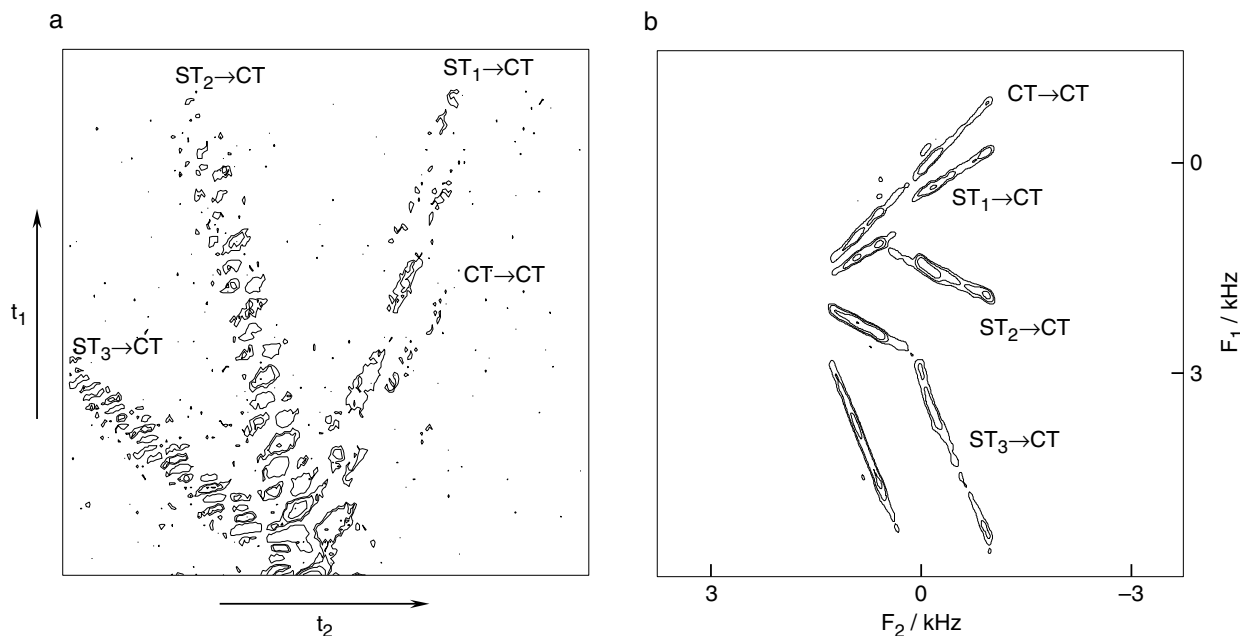**FIG. 9.** ^{45}Sc (97.2 MHz) NMR of Sc$_2$(SO$_4$)$_3 \cdot$ 5H$_2$O. (a) Two-dimensional time-domain data set and (b) corresponding two-dimensional STMAS NMR spectrum recorded using the pulse sequence shown in Fig. 1a. The spectrum is the result of the averaging of 32 transients with a recycle interval of 1 s for each of 128 t_1 increments of 50 μs. The MAS rate was 20 kHz. In (a) negative contour levels are omitted for clarity, whilst in (b) contour levels are shown at 8, 16, 32, and 64% of the maximum intensity. No widely accepted ^{45}Sc chemical shift reference exists and the F_1 and F_2 scales give the offset from the transmitter frequency in kHz.

observed, centered at $\delta_2 \approx 8$ and 65 ppm, corresponding to octahedrally and tetrahedrally coordinated aluminum, respectively (27). Unfortunately, however, owing to the large frequency difference between the two sites and the duration of the shortest t_1 interval being $\sim\tau_R$ rather than 0, this spectrum is difficult to "phase" and the two sites appear with amplitudes that have opposite sign. In addition to the anisotropic quadrupolar broadening, lying along an axis with gradient $+7/24$, there is evidence for additional broadening mechanisms in both resonances, reflecting the amorphous nature of the sample. For a spin $I = 5/2$ $ST_1 \rightarrow CT$ lineshape, a distribution of isotropic chemical shifts would lead to a broadening in the two-dimensional spectrum along an axis of gradient $+1$, while a distribution of quadrupolar parameters would result in a broadening along $-1/8$. The two ^{27}Al resonances in the spectrum in Fig. 8 display evidence of distributions in both isotropic chemical shift and quadrupolar parameters. Furthermore, the two lineshapes are very similar in size and shape, indicating that the distributions are of similar magnitude in each. As has been demonstrated in the analysis of MQMAS spectra, it is possible to obtain estimates of the size of the distributions present using a lineshape-fitting procedure (25).

STMAS OF SPIN $I = 7/2$ NUCLEI

Nuclei with a spin quantum number of $I = 7/2$ possess three different types of satellite transition: ST_1 with $m_I = \pm 1/2 \leftrightarrow \pm 3/2$, ST_2 with $m_I = \pm 3/2 \leftrightarrow \pm 5/2$, and ST_3 with $m_I = \pm 5/2 \leftrightarrow \pm 7/2$. Figure 9a shows a two-dimensional ^{45}Sc ($I = 7/2$) FID of $Sc_2(SO_4)_3 \cdot 5H_2O$, recorded using the shifted-echo sequence in Fig. 1a. Four echoes are observed: the $CT \rightarrow CT$ and $ST_1 \rightarrow CT$ echo signals moving forward in t_2 as t_1 increases, and two (anti)echo signals, $ST_2 \rightarrow CT$ and $ST_3 \rightarrow CT$, moving backward in t_2 with increasing t_1. Figure 9b shows the two-dimensional STMAS spectrum resulting from the Fourier transformation of the time-domain data set in Fig. 9a. In addition to the $CT \rightarrow CT$ peaks lying along the diagonal, all three sets of satellite transitions are observed lying along gradients of $+28/45$, $-23/45$, and $-108/45$, for $ST_1 \rightarrow CT$, $ST_2 \rightarrow CT$, and $ST_3 \rightarrow CT$ transitions, respectively. For each set of $ST_n \rightarrow CT$ peaks, three ridge lineshapes may be seen, corresponding to the three crystallographically distinct ^{45}Sc nuclei present in $Sc_2(SO_4)_3 \cdot 5H_2O$, with C_Q values of 5.2, 4.3, and 4.5 MHz and relative site populations $1 : 1 : 2$ (21).

Figure 10 compares ^{45}Sc isotropic projections obtained from split-t_1 STMAS spectra of $Sc_2(SO_4)_3 \cdot 5H_2O$, recorded with the pulse sequence shown in Fig. 1b, with k, k', and k'' as described in the figure caption. It can be seen that the frequency dispersion in Fig. 10a, resulting from the $ST_1 \rightarrow CT$ transitions, is considerably smaller than that obtained in Figs. 10b and 10c, arising from $ST_2 \rightarrow CT$ and $ST_3 \rightarrow CT$ transitions, respectively. Furthermore, only two resonances are resolved in the first spectrum, emphasizing the lower shift dispersion. Table 2 predicts absolute chemical shift scaling factors of 0.233, 1.000, and 1.000 for Figs. 10a, 10b, and 10c, respectively, and it is clear that
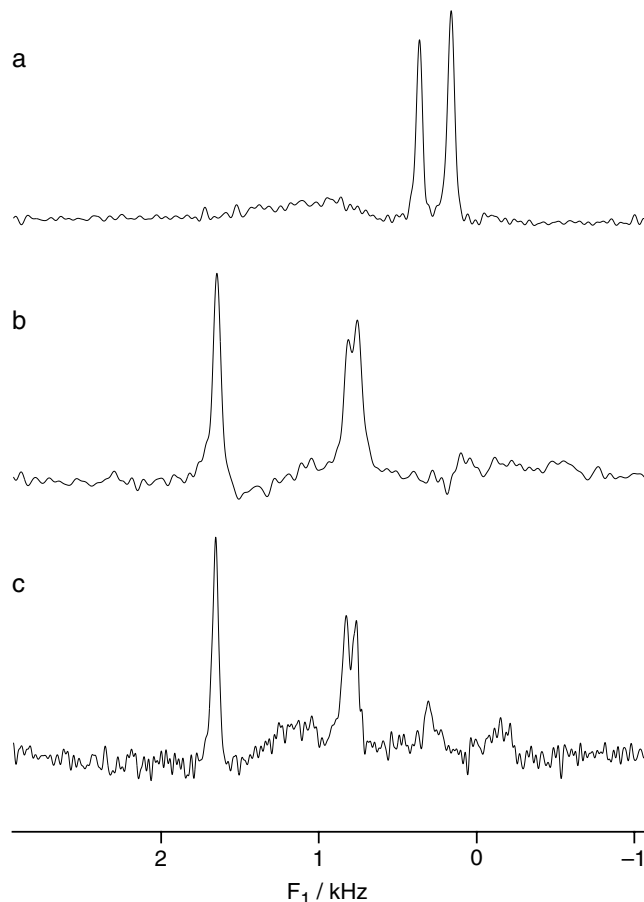

FIG. 10. ^{45}Sc (97.2 MHz) NMR of $Sc_2(SO_4)_3 \cdot 5H_2O$. Isotropic projections of two-dimensional STMAS NMR spectra recorded using the split-t_1 pulse sequence shown in Fig. 1b, with (a) $k = 45/73$, $k' = 0$, and $k'' = 28/73$, (b) $k = 45/68$, $k' = 23/68$, and $k'' = 0$ and (c) $k = 45/153$, $k' = 108/153$, and $k'' = 0$. In each case, 32 transients were averaged with a recycle interval of 1 s for (a) 477 t_1 increments of 81.1 μs, (b) 512 t_1 increments of 75.6 μs, and (c) 227 t_1 increments of 170.0 μs. The MAS rate was 20 kHz. The F_1 scale shows the offset from the transmitter frequency.

the frequency dispersions in Figs. 10b and 10c are identical. However, the linewidths in Fig. 10c appear slightly smaller than those in Fig. 10b, even though all spectra were recorded with identical maximum values of t_1, resulting in a slight increase in resolution.

^{59}Co NMR studies are often hampered by the presence of large quadrupolar interactions and large chemical shift anisotropies (28). For MQMAS NMR, in particular, a high spinning frequency, often required when the quadrupolar or CSA interactions are large, results in poor multiple-quantum filtration efficiency (19). Although the signal intensity in an STMAS experiment still possesses a dependence upon the quadrupolar interaction, the significant enhancement in signal intensity, coupled with the very small dependence upon the spinning frequency shown above, appears to offer a viable approach for nuclei such as ^{59}Co.
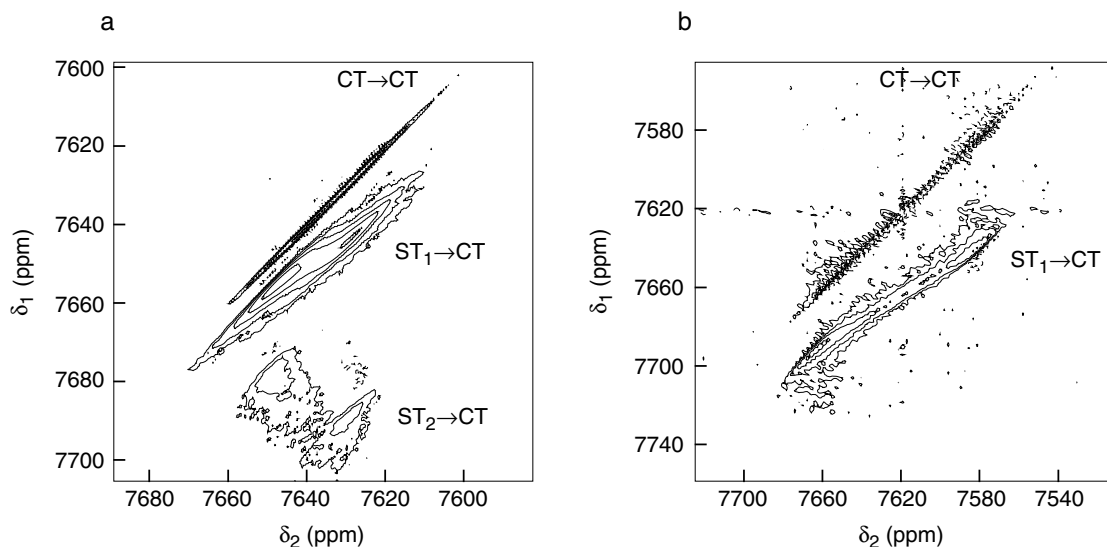
FIG. 11. ^{59}Co NMR of Na$_3$Co(NO$_2$)$_6$. Two-dimensional STMAS spectra recorded using the pulse sequence shown in Fig. 1a at static magnetic field strengths, B_0, of (a) 9.4 T (^{59}Co: $\omega_0/2\pi = 94.5$ MHz) and (b) 4.7 T (^{59}Co: $\omega_0/2\pi = 47.3$ MHz). In (a) 576 and (b) 128 transients were averaged with a recycle interval of 1 s for each of 128 t_1 increments of 50 μs. The MAS rate was (a) 20 kHz and (b) 10 kHz. Contour levels are shown at (a) 4, 8, 16, 32, and 64% and (b) 8, 16, 32, and 64% of the maximum intensity. All ppm scales are referenced to a saturated solution of K$_3$Co(CN)$_6$ (aq).

Figure 11a shows a two-dimensional ^{59}Co STMAS spectrum of Na$_3$Co(NO$_2$)$_6$, recorded using the pulse sequence shown in Fig. 1a. Peaks corresponding to CT $\rightarrow$ CT and ST$_1$ $\rightarrow$ CT transitions may be seen, lying along +1 and +28/45, respectively. The peak arising from the ST$_2$ $\rightarrow$ CT transition can also be seen at lower contour levels, along −23/45. It is clear that the single ^{59}Co ST$_1$ $\rightarrow$ CT peak also possesses a considerable broadening along the +1 axis. It has recently been shown that high-resolution "isotropic" MQMAS NMR spectra of half-integer quadrupolar nuclei are broadened by anisotropic second-order quadrupolar–dipolar cross-term interactions. Such interactions, occurring between two quadrupolar nuclei, will also broaden STMAS spectra, with the cross-term broadening appearing along the +1 axis (29–31). An alternative explanation is that the additional broadening is a result of a distribution of isotropic chemical shifts or susceptibilities, which would also lie along this axis. To determine the true nature of the interaction it is necessary to record spectra at differing magnetic field strengths. Figure 11b shows a two-dimensional ^{59}Co STMAS spectrum of Na$_3$Co(NO$_2$)$_6$, recorded at 4.7 T. Although the anisotropic quadrupolar broadening (along a gradient of +28/45) has increased owing to the lower static magnetic field strength, the broadening along +1 has significantly decreased. This suggests that the broadening mechanism responsible for the linewidth in this sample is a distribution of isotropic chemical shifts, i.e., an interaction proportional to B_0, rather than a second-order cross-term interaction which would exhibit an inverse relationship with B_0. Further support for this idea is provided by the triple-quantum ^{59}Co MAS spectrum recorded at 9.4 T (not shown), which shows the additional broadening along the +3 gradient.

STMAS OF SPIN $I = 9/2$ NUCLEI

Figure 12a shows a two-dimensional ^{93}Nb STMAS NMR spectrum of LiNbO$_3$, recorded with the pulse sequence shown in Fig. 1a. Three ridge-like lineshapes are observed: a CT $\rightarrow$ CT peak along +1, a ST$_1$ $\rightarrow$ CT peak along +55/72, and a ST$_2$ $\rightarrow$ CT peak along +1/18. All three arise from time-domain echo signals as is indicated in Table 1 by the positive signs of the STMAS ratios. In order to observe ridges arising from time-domain antiecho signals, the ^{93}Nb STMAS NMR spectrum shown in Fig. 12b was recorded using a simple two-pulse sequence with selection of $p = -1$ coherences in t_1 (9). Although pure-phase lineshapes are not yielded by this experiment, it is possible to observe ridge lineshapes corresponding to the ST$_3$ $\rightarrow$ CT and ST$_4$ $\rightarrow$ CT peaks lying along −9/8 and −25/9, respectively. Owing to the large quadrupole interaction ($C_Q = 22.1$ MHz) (32), these peaks lie outside the spectral width (determined by rotor-synchronized acquisition) and are folded. In particular, the latter transition, ST$_4$ $\rightarrow$ CT, is very broad in the δ_1 dimension, starting toward the bottom half of the spectral width, folding for a second time to emerge at the top of the spectrum and crossing the ST$_3$ $\rightarrow$ CT transition (which has folded only once).

Figure 13a shows a two-dimensional ^{93}Nb STMAS NMR spectrum of a mixture of LiNbO$_3$ and NaNbO$_3$, recorded with the split-t_1 shifted-echo pulse sequence in Fig. 1b, with $k = 72/127$, $k' = 0$, and $k'' = 55/127$. In addition to the CT $\rightarrow$ CT peak, two further ridge-like lineshapes are observed, corresponding to the ST$_1$ $\rightarrow$ CT transitions in LiNbO$_3$ and NaNbO$_3$. The LiNbO$_3$ signal, $\delta_1 \approx -130$ ppm, exhibits a narrow ridge-like lineshape parallel to the δ_2 axis. However, although the
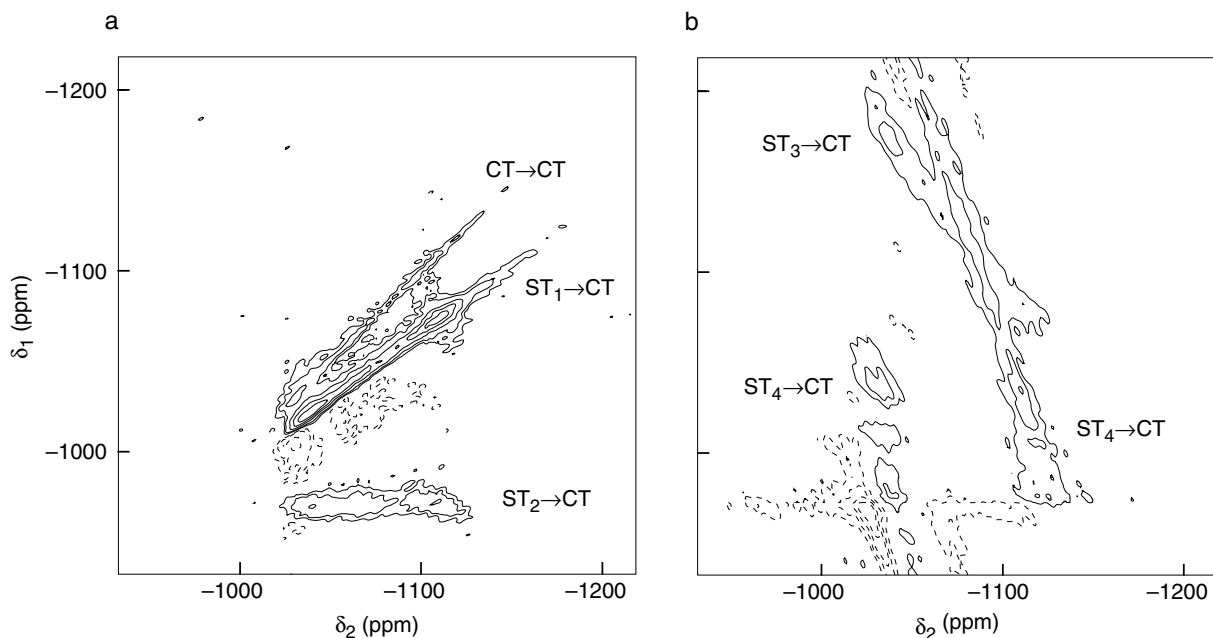
FIG. 12. ^{93}Nb (97.8 MHz) NMR of LiNbO$_3$. Two-dimensional STMAS spectra were recorded using (a) the pulse sequence shown in Fig. 1a and (b) the two-pulse sequence (solid pathway) of Fig. 1a in Ref. (9). In each case, 256 transients were averaged with a recycle interval of 500 ms for each of (a) 64 and (b) 32 t_1 increments of 35.7 μs. The MAS rate was 28 kHz. Contour levels are shown at (a) 10, 20, 40, 60, and 80% and (b) 20, 40, 60, and 80% of the maximum intensity. All ppm scales are referenced to a saturated solution of NbCl$_5$ in "wet" acetonitrile.
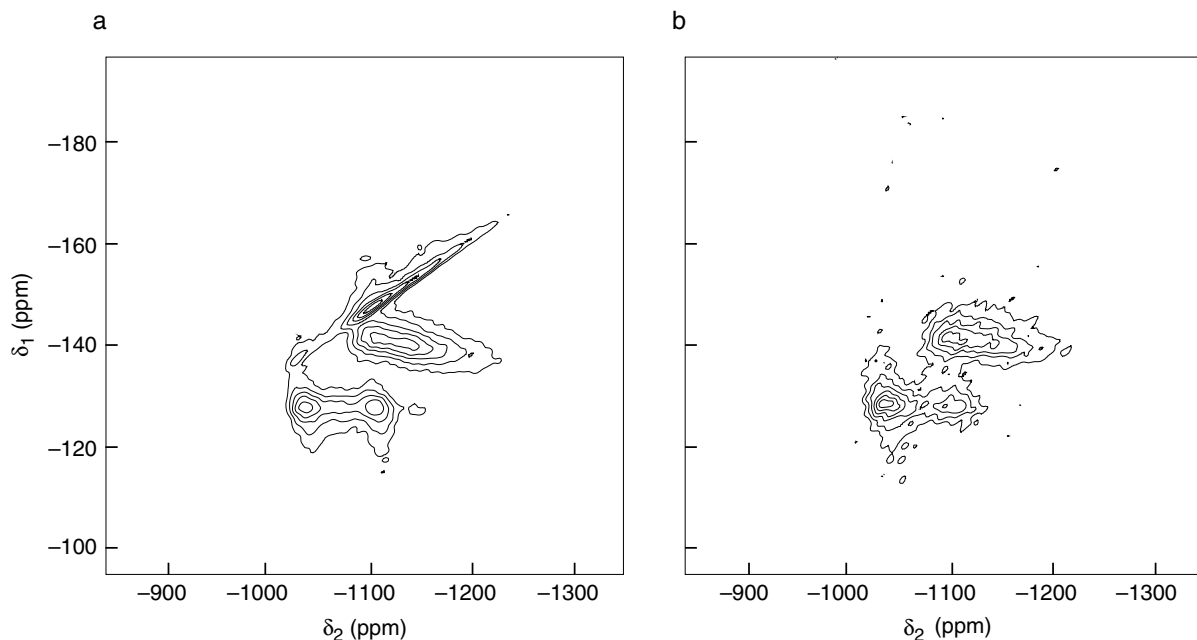

FIG. 13. ^{93}Nb (97.8 MHz) NMR of a mixture of LiNbO$_3$ and NaNbO$_3$. Two-dimensional (a) STMAS and (b) triple-quantum MAS NMR spectra recorded using (a) the split-t_1 pulse sequence shown in Fig. 1b with $k = 72/127$, $k' = 0$, and $k'' = 55/127$, and (b) a triple-quantum split-t_1 sequence (14). In (a) 256 and (b) 768 transients were averaged with a recycle interval of 500 ms for each of 96 t_1 increments of 52.9 μs. The MAS rate was 33.3 kHz. Contour levels are shown at 15, 30, 45, 60, 75, and 90% of the maximum intensity in both cases. All ppm scales are referenced to a saturated solution of NbCl$_5$ in "wet" acetonitrile.

NaNbO$_3$ lineshape, at $\delta_1 \approx -140$ ppm, does appear approximately parallel to δ_2, there is evidence for additional broadening mechanisms along other axes. Distributions in the chemical shift and quadrupolar interactions would lead to broadenings along axes with gradients $+1$ and $+5/8$ in a spin $I = 9/2$ ST$_1 \rightarrow$ CT spectrum. In a ST$_1 \rightarrow$ CT split-t_1 spectrum, therefore, these broadenings will appear along $+17/127$ and $-80/127$, respectively. The STMAS spectrum in Fig. 13a suggests that small distributions in these interactions are present in NaNbO$_3$.

Figure 13b shows a two-dimensional split-t_1 ^{93}Nb triple-quantum MAS NMR spectrum of the LiNbO$_3$–NaNbO$_3$ mixture. Two distinct lineshapes are observed, with again that corresponding to NaNbO$_3$ displaying additional broadening. Comparison of the isotropic (δ_1) dimensions in the STMAS and MQMAS spectra shows that the absolute chemical shift dispersion is identical, as predicted in Table 2, and, therefore, both experiments should yield similar resolution. However, it should be noted that the signal intensity in the STMAS spectrum (Fig. 13a) is 1.8 times greater than that of the MQMAS spectrum and was recorded in 3.4 h compared with 10.2 h for the MQMAS spectrum. The relatively large sensitivity difference in this case is a consequence of the high spinning speed ($\nu_R = 33.3$ kHz) employed in both experiments owing to the large quadrupolar interactions of the two components in the mixture. As shown in Fig. 5, the sensitivity of MQMAS is significantly decreased at high MAS frequencies, whereas that of STMAS is unaffected.

CONCLUSIONS

In view of the sensitivity advantage of using a purely single-quantum technique, STMAS offers a very promising alternative to MQMAS for obtaining high-resolution NMR spectra of quadrupolar nuclei. In our experience, STMAS experiments (ST$_1 \rightarrow$ CT) yield between three and six times the signal-to-noise ratio of triple-quantum MAS experiments recorded in the same total experiment time and with the same limiting resolution. These experimental comparisons were made without using methods that are known to enhance MQMAS sensitivity by up to 100% (*4–6*) but we believe this to be the most even-handed approach since similar methods can be envisaged for STMAS. We have also demonstrated that the sensitivity of the STMAS experiment is much less dependent upon the MAS rate than that of the MQMAS experiment, with the result that especially favorable sensitivity gains are expected at higher spinning frequencies. However, the technical requirements of STMAS, particularly those of an accurately set magic angle and a stable spinning rate, should be noted carefully, although both requirements are alleviated (at the cost of some sensitivity) in the new SCAM-STMAS experiment (*33*). We have discussed the experimental implementation of STMAS on a spin $I = 3/2$ system and demonstrated the optimization of the pulse durations in a shifted-echo STMAS experiment.

The application of STMAS to nuclei with spin quantum number $I > 3/2$ has also been considered, and we have demonstrated the possibility of using each different set of satellite transitions (i.e., ST$_1$, ST$_2$) in an STMAS experiment. We have shown that the absolute chemical shift scaling factor obtained in each of these experiments is different, with a maximum value of 1.000. Although this change in scaling factor does not necessarily lead to a resolution enhancement owing to additional changes in linewidth, we have demonstrated (in Fig. 10) a case where a real and significant increase in resolution is observed. It should be noted that there is also a reduction in sensitivity as the satellite-transition order increases. STMAS appears to be a very promising technique for systems with low inherent sensitivity (e.g., ^{17}O NMR) or for systems where a large quadrupolar interaction or large CSA exists, requiring a high spinning frequency to be used. Additionally, we have also demonstrated the use of STMAS on amorphous systems and envisage further applications in this area.

REFERENCES

1. K. T. Mueller, B. Q. Sun, G. C. Chingas, J. W. Zwanziger, T. Terao, and A. Pines, *J. Magn. Reson.* **86,** 470 (1990).

2. A. Samoson, E. Lippmaa, and A. Pines, *Mol. Phys.* **65,** 1013 (1998).

3. L. Frydman and J. S. Harwood, *J. Am. Chem. Soc.* **117,** 5367 (1995).

4. G. Wu, D. Rovnyak, and R. G. Griffin, *J. Am. Chem. Soc.* **118,** 9326 (1996).

5. P. K. Madhu, A. Goldburt, L. Frydman, and S. Vega, *Chem. Phys. Lett.* **307,** 41 (1999).

6. A. P. M. Kentgens and R. Verhagen, *Chem. Phys. Lett.* **300,** 435 (1999).

7. Z. Gan, *J. Am. Chem. Soc.* **122,** 3242 (2000).

8. Z. Gan, *J. Chem. Phys.* **114,** 10845 (2001).

9. K. J. Pike, S. E. Ashbrook, and S. Wimperis, *Chem. Phys. Lett.* **345,** 400 (2001).

10. M. E. Smith and E. R. H. van Eck, *Prog. NMR Spectrosc.* **34,** 159 (1999).

11. P. J. Grandinetti, J. H. Baltisberger, A. Llor, Y. K. Lee, U. Werner, M. A. Eastman, and A. Pines, *J. Magn. Reson. A* **103,** 72 (1993).

12. D. Massiot, B. Touzo, D. Trumeau, J. P. Coutures, J. Virlet, P. Florian, and P. J. Grandinetti, *Solid State NMR* **6,** 73 (1996).

13. S. P. Brown, S. J. Heyes, and S. Wimperis, *J. Magn. Reson. A* **119,** 280 (1996).

14. S. P. Brown and S. Wimperis, *J. Magn. Reson.* **124,** 279 (1997).

15. S. P. Brown and S. Wimperis, *J. Magn. Reson.* **128,** 42 (1997).

16. S. P. Brown, S. E. Ashbrook, and S. Wimperis, *J. Phys. Chem. B* **103,** 812 (1999).

17. Z. Gan, *in* "43rd Rocky Mountain Conference on Analytical Chemistry, Colorado," 2001.

18. A. F. Mehlkopf, D. Korbee, T. A. Tiggleman, and R. Freeman, *J. Magn. Reson.* **58,** 315 (1984).

19. J. P. Amoureux, M. Pruski, D. P. Lang, and C. Fernandez, *J. Magn. Reson.* **131,** 170 (1998).

20. J. P. Amoureux and C. Fernandez, *Solid State NMR* **10,** 211 (1998).

21. K. J. Pike, R. P. Malde, S. E. Ashbrook, J. McManus, and S. Wimperis, *Solid State NMR* **16,** 203 (2000).

22. S. E. Ashbrook, S. P. Brown, and S. Wimperis, *Chem. Phys. Lett.* **288,** 509 (1998).

23. A. P. M. Kentgens, *Geoderma* **80,** 271 (1997).

24. M. E. Smith, *Appl. Magn. Reson.* **4,** 1 (1993).

25. J. McManus, S. E. Ashbrook, K. J. D. MacKenzie, and S. Wimperis, *J. Non-Cryst. Solids* **282,** 278 (2001).

26. S. E. Ashbrook, K. J. D. MacKenzie, and S. Wimperis, *Solid State NMR* **20,** 87 (2001).

27. H. Kraus, R. Prins, and A. P. M. Kentgens, *J. Phys. Chem.* **100,** 16336 (1996).

28. T. Charpentier and J. Virlet, *Solid State NMR* **12,** 227 (1998).

29. J. McManus, R. Kemp-Harper, and S. Wimperis, *Chem. Phys. Lett.* **311,** 292 (1999).

30. G. Wu and K. Yamada, *Chem. Phys. Lett.* **313,** 519 (1999).

31. S. Wi and L. Frydman, *J. Chem. Phys.* **112,** 3248 (2000).

32. S. Prasad, P. Zhao, J. Huang, J. J. Fitzgerald, and J. S. Shore, *Solid State NMR* **19,** 45 (2001).

33. S. E. Ashbrook and S. Wimperis, submitted for publication.